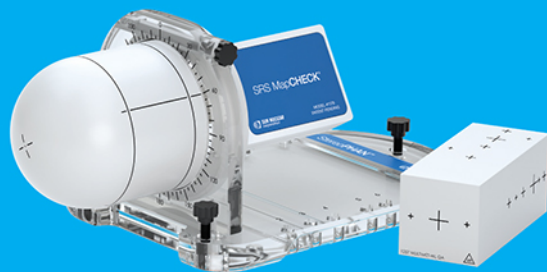


# Sun Nuclear at **AAPM 2022** **Booth #4000**



Stereophan™, SRS MapCHECK®, MultiMet-WL Cube

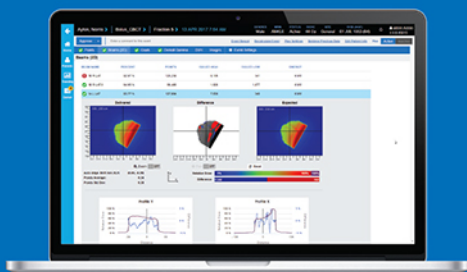
**NEW**



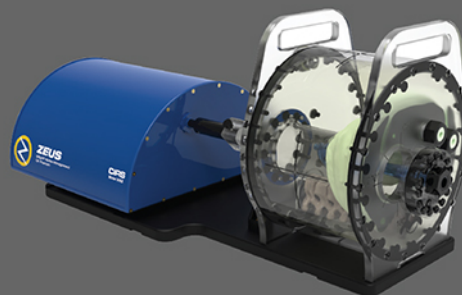
SunSCAN™ 3D Water Scanning System

At the AAPM Annual Meeting, July 10 - 13, Sun Nuclear and CIRS will combine to feature our portfolio of smarter Quality Management solutions. Join us for our annual symposium, daily in-booth talks, and product demonstrations.

**[sunnuclear.com/aapm](http://sunnuclear.com/aapm)**



SunCHECK™ Patient



Zeus MRgRT Motion Management QA Phantom

# Comparison of voxel S-value methods for personalized voxel-based dosimetry of $^{177}\text{Lu}$ -DOTATATE

Keon Min Kim<sup>1,2</sup> | Min Sun Lee<sup>3</sup> | Min Seok Suh<sup>4,5</sup> |  
 Haniff Shazwan Muhd Safwan Selvam<sup>6</sup> | Teik Hin Tan<sup>6</sup> | Gi Jeong Cheon<sup>4,5</sup> |  
 Keon Wook Kang<sup>4,5,7</sup> | Jae Sung Lee<sup>1,2,4,5</sup>

<sup>1</sup> Interdisciplinary Program in Bioengineering, Seoul National University Graduate School, Seoul, Korea

<sup>2</sup> Integrated Major in Innovative Medical Science, Seoul National University Graduate School, Seoul, Korea

<sup>3</sup> Korea Atomic Energy Research Institute, Daejeon, Korea

<sup>4</sup> Department of Nuclear Medicine, Seoul National University College of Medicine, Seoul, Korea

<sup>5</sup> Institute of Radiation Medicine, Medical Research Center, Seoul National University, Seoul, Korea

<sup>6</sup> Nuclear Medicine Centre, Sunway Medical Centre, Selangor, Malaysia

<sup>7</sup> Bio-MAX Institute, Seoul National University, Seoul, Korea

## Correspondence

Jae Sung Lee, Department of Nuclear Medicine, Seoul National University College of Medicine, 103 Daehak-ro, Jongno-gu, Seoul 03080, Korea.  
 Email: [jaes@snu.ac.kr](mailto:jaes@snu.ac.kr)

## Funding information

National Research Foundation of Korea (NRF); Korean Ministry of Science and ICT, Grant/Award Number: 2020M2D9A1093989; Sunway Medical Centre

## Abstract

**Purpose:** Voxel-based dosimetry is potentially accurate than organ-based dosimetry because it considers the anatomical variations in each individual and the heterogeneous radioactivity distribution in each organ. Here, voxel-based dosimetry for  $^{177}\text{Lu}$ -DOTATATE therapy was performed using single and multiple voxel S-value (VSV) methods and compared with Monte Carlo simulations. To verify these methods, we adopted sequential  $^{177}\text{Lu}$ -DOTATATE single-photon emission computed tomography and X-ray computed tomography (SPECT/CT) dataset acquired from Sunway Medical Centre using the major vendor's SPECT/CT scanner (Siemens Symbia Intevo).

**Methods:** The administered activity of  $^{177}\text{Lu}$ -DOTATATE was  $7.99 \pm 0.36$  GBq. SPECT/CT images were acquired 0.5, 4, 24, and 48 h after injection in Sunway Medical Centre. For the multiple VSV method, VSV kernels of  $^{177}\text{Lu}$  in media with various densities were generated by Geant4 Application for Emission Tomography (GATE) simulation first. The second step involved the convolution of the time-integrated activity map with each kernel to produce medium-specific dose maps. Third, each medium-specific dose map was masked using binary medium masks, which were generated from CT-based density maps. Finally, all masked dose maps were summed to generate the final dose map. VSV methods with four different VSV sets (1, 4, 10, and 20 VSVs) were compared. Voxel-wise density correction for the single VSV method was also performed. The absorbed doses in the kidneys, bone marrow, and tumors were analyzed, and the relative errors between the VSV and Monte Carlo simulation approaches were estimated. Organ-based dosimetry using Organ Level Internal Dose Assessment/EXponential Modeling (OLINDA/EXM) was also compared.

**Results:** The accuracy of the multiple VSV approach increased with the number of dose kernels. The average dose estimation errors of a single VSV with density correction and 20 VSVs were less than 6% in most cases, although organ-based dosimetry using OLINDA/EXM yielded an error of up to 123%. The advantages of the single VSV method with density correction and the 20 VSVs over organ-based dosimetry were most evident in bone marrow and bone-metastatic tumors with heterogeneous medium properties.

**Conclusion:** The single VSV method with density correction and multiple VSV method with 20 dose kernels enabled fast and accurate radiation dose estimation. Accordingly, voxel-based dosimetry methods can be useful for managing administration activity and for investigating tumor dose responses to further increase the therapeutic efficacy of  $^{177}\text{Lu}$ -DOTATATE.

**KEYWORDS**

dose kernel, Monte Carlo simulation, neuroendocrine tumor, radiation dosimetry, radionuclide therapy

## 1 | INTRODUCTION

$^{177}\text{Lu}$ -octreotate ( $^{177}\text{Lu}$ -DOTATATE) peptide receptor radionuclide therapy is an important treatment option for somatostatin receptor type-2 positive neuroendocrine tumors (NETs).<sup>1</sup>  $^{177}\text{Lu}$  emits beta particles with a maximum energy of 498 keV, which is effective in destroying malignant tumor cells and yields a short range in soft tissue ( $\sim 0.2$  mm on average).<sup>2</sup> Therefore, the therapeutic efficiency is high and there are few side-effects on normal tissue. In addition,  $^{177}\text{Lu}$  emits gamma rays with 208 keV (11%) and 113 keV (6.4%) energies, allowing gamma camera imaging to visualize the distribution of radiopharmaceuticals. Single-photon emission computed tomography and X-ray computed tomography (SPECT/CT) systems are also widely used for quantitative  $^{177}\text{Lu}$  imaging.

Voxel-based dosimetry based on 3D volumetric data is potentially accurate than organ-based dosimetry because it considers the anatomical variations in each individual and heterogeneous radioactivity distribution in each organ. Among the several approaches of voxel-based dosimetry, the dose point kernel method and the single voxel *S*-value (VSV) approach<sup>3,4</sup> have limited accuracy because they assume that the body tissue is composed of water-equivalent materials only. This unrealistic assumption inevitably leads to dose estimation errors in non-water-equivalent tissues, such as the lungs and bones. To compensate for the dose errors in heterogeneous media when using the conventional single VSV method, voxel-wise density correction was suggested.<sup>5</sup> The accuracy improvement through density correction was illustrated at the voxel level for  $^{177}\text{Lu}$ ,  $^{90}\text{Y}$ , and  $^{131}\text{I}$ . The effect of voxel-wise density correction was also demonstrated for bone-metastasis dosimetry in patients who received  $^{177}\text{Lu}$  labeled prostate-specific membrane antigen (PSMA) therapy.<sup>6</sup> The use of Monte Carlo simulation allows for a more accurate dose estimation.<sup>7–9</sup> However, the long computation time required to perform the simulation is a hurdle that prevents the routine application of this approach. Recently, we have proposed a new voxel-based approach that uses multiple VSVs for heterogeneous media with nonuniform activity distributions.<sup>10</sup> This method enables fast personalized dosimetry at the whole-body level, yielding dosimetry measurements comparable to those achieved using the direct Monte Carlo approach while significantly reducing the computation time. However, this has been validated for  $^{68}\text{Ga}$  positron emission tomography (PET)/CT data only.

After the application of the  $^{177}\text{Lu}$ -DOTATATE therapy, retrospective dosimetry measurements are required to assess the absorbed dose delivered to tumors and organs at risk, such as the kidney and bone marrow. The MIRDC Committee provides general guidelines for  $^{177}\text{Lu}$ -DOTATATE dosimetry<sup>11</sup>; however, voxel-based dosimetry methods have not been considered. Although several studies have reported estimates of absorbed doses for  $^{177}\text{Lu}$ -DOTATATE therapy,<sup>12–20</sup> these estimates were measured based only on organ-based dosimetry. However, as the number of clinical dosimetry protocols including  $^{177}\text{Lu}$  SPECT/CT scans is increasing, there is growing interest in personalized voxel-based dosimetry in  $^{177}\text{Lu}$ -DOTATATE therapy.

In this study, SPECT/CT-based dosimetry for  $^{177}\text{Lu}$ -DOTATATE therapy was performed at voxel level and the absorbed dose in two critical organs (kidney and bone marrow) and the primary and metastatic tumors were estimated. In particular, the multiple VSV method with different numbers of dose kernels and the single VSV method with density correction were applied and compared with the Monte Carlo simulation, which is regarded as the reference method, and organ-based dosimetry.

## 2 | MATERIALS AND METHODS

### 2.1 | Data acquisition and processing

We analyzed  $^{177}\text{Lu}$ -DOTATATE SPECT/CT dataset acquired using the SPECT/CT system of the major provider (Sunway Medical Centre (SMC), Selangor, Malaysia). The study protocol and patient demographic data are summarized in Tables 1 and 2, respectively. The retrospective use of the scan data and waiver of consent were approved by the Institutional Review Board of Sunway Medical Centre. Informed consent was obtained from all individual participants included in the study.

At SMC, four time points of SPECT/CT images were acquired for 20 patients who received the first cycle  $^{177}\text{Lu}$ -DOTATATE treatment. These images were acquired at 0.5, 4, 24, and 48 h after intravenous injection of  $^{177}\text{Lu}$ -DOTATATE using the Siemens Symbia Intevo SPECT/CT system with medium energy collimator. Multi-bed scan (two to three beds) from neck to thigh took approximately 25–40 min (32 views, 25 s per view, and 13.3 min per bed). The matrix size of the reconstructed images was  $512 \times 512$  for CT and  $103 \times 103$  for SPECT. The total number of CT and SPECT slices were variable because of the use of different slice thickness

**TABLE 1**  $^{177}\text{Lu}$ -DOTATATE single-photon emission computed tomography and X-ray computed tomography (SPECT/CT) dataset

<b>Sunway Medical Centre</b>	
No. of scans	20
Administered activity (GBq)	$7.99 \pm 0.36$
Device	Siemens Symbia Intevo
Protocol	0.5, 4, 24, 48 h post-injection
CT image	$512 \times 512$ , variable slice numbers
SPECT image	$103 \times 103$ , variable slice numbers ( $4.88 \times 4.88 \times 4.88 \text{ mm}^3$ )
Reconstruction	OSCGM (AC, SC)

Abbreviations: AC, attenuation correction; OSCGM, ordered subset conjugate gradient minimizer; SC, scatter correction.

**TABLE 2** Demographic data of the patients

Patient no.	Sex	Height (cm)	Weight (kg)	Diagnosis	Injection dose (GBq)
1	F	158	59	Pancreatic NET Liver metastasis	8.88
2	F	153	57	Rectal NET Liver and bone metastasis	7.66
3	F	164	66	Rectal NET Liver, lymph nodal, and bone metastasis	8.10
4	M	174	69	Rectal NET Liver, lymph nodal, and bone metastasis	7.77
5	M	184	87	Duodenal NET	7.73
6	F	144	47	Rectal NET Liver and bone metastasis	7.47
7	M	177	76	Pancreatic NET Lymph nodal metastasis	7.77
8	M	163	51	Pancreatic NET Liver, lymph nodal, and bone metastasis	8.14
9	F	161	54	Pancreatic NET Lymph nodal metastasis	8.66
10	F	153	72	Right kidney NET Lymph nodal metastasis	7.55
11	F	158	59	Pancreatic NET Liver and lymph nodal metastasis	7.81
12	M	156	51	Pancreatic NET Liver and lymph nodal metastasis	7.81
13	M	167	62	Functioning insulinoma Liver and pancreatic metastasis	8.14
14	M	168	73	Pancreatic NET Liver, lymph nodal, and bone metastasis	7.99
15	F	161	59	Pancreatic NET Liver metastasis	7.51
16	F	159	53	Sacral paraganglioma	8.18
17	F	162	79	Rectal NET Liver and bone metastasis	8.14
18	F	153	66	Pancreatic NET	8.14
19	M	161	60	Lung carcinoid Liver, lymph nodal, and bone metastasis	8.07
20	M	166	61	Pancreatic NET Liver metastasis	8.25

Abbreviations: F, female; M, male; NET, neuroendocrine tumor.

(3, 5, and 10 mm for CT image) in different time points. Despite variable in slices, the SPECT voxel size was equal ( $4.88 \times 4.88 \times 4.88 \text{ mm}^3$ ). Ordered subset conjugate gradient minimizer (OSCGM) algorithm including attenuation correction (AC) and scatter correction (SC) was used for SPECT reconstruction. The number of iterations and subsets were eight each. A 12 mm Gaussian filter was applied. A triple energy window approach was used for SC. Briefly, the peak energy window was set at 208 keV with 20% window, and upper and lower 10% scatter windows were set.

For the activity calibration of the SPECT system, a built-in system method of Siemens products called “Broad Quantification” was used. Broad Quantification is divided into two procedures, point source sensitivity calibration and volume sensitivity calibration.<sup>177</sup>Lu point source of 5–10 mCi was used for point source calibration and a uniform cylinder phantom filled with <sup>177</sup>Lu solution (total activity = 10–20 mCi) was used for the volume sensitivity calibration.

For regional dose calculation, the volumes of interest (VOIs) were drawn on the kidney, bone marrow, and tumors. The dose delivered to the bone marrow was estimated from the VOIs of the lumbar spine (L-spine).<sup>21</sup> The VOIs of the entire lumbar spine were delineated first. Then, the cortical bone area was removed by applying appropriate Hounsfield unit (HU) thresholds for each patient. It was assumed that these VOIs without hard bone are the active marrow region. The existence of microstructures (i.e., trabecular bone and yellow marrow regions) within these VOIs was not considered in this study. The VOIs on the kidney and bone marrow were manually drawn using 3D Slicer software.<sup>22</sup> For tumor regions, the VOIs were drawn on SPECT/CT images using the PET-edge technique provided by MIM software (MIM Software Inc., Cleveland, OH, USA).

## 2.2 | Monte Carlo simulation

Dose estimations based on Monte Carlo simulations were considered as the reference method. Geant4 Application for Emission Tomography (GATE) v.8.2 was used for the simulation.<sup>23</sup> Prior to the simulation, the CT images were resampled to assign them the same voxel size as that of the SPECT images using in-house MATLAB 2021b code. Sequential SPECT/CT images were then co-registered using a nonlinear registration algorithm provided by the Elastix software.<sup>24</sup> CT images acquired at different time points were registered to the first or second time point image (reference CT), and the transformation parameters obtained from CT image registration were applied to SPECT images. Finally, we generated time-integrated activity maps from the registered sequential SPECT images using trapezoidal sum-

mation, as follows<sup>25</sup>:

$$\bar{A} = \sum_{i=0}^3 \frac{1}{2} (A_i + A_{i+1}) \Delta t_i + \int_{t_4}^{\infty} A_4 e^{-\lambda t} dt. \quad (1)$$

where  $A_i$  is the activity ( $A_0 = 0$ ) in each voxel of the  $i$ th SPECT images acquired at  $t_i$ ,  $\Delta t_i = t_{i+1} - t_i$ , and  $\lambda$  is the physical decay factor of <sup>177</sup>Lu.

Time-integrated activity maps and reference CT images were used as the voxelized source and phantom for the GATE simulation. For voxelized phantoms, the CT HU was converted into density ( $\text{g/cm}^3$ ) using a material database file for GATE running.<sup>26</sup> GATE dosimetry was performed by executing the “DoseActor” tool, which provides a voxel-wise energy deposition map (unit: MeV) and dose map (unit: Gy) in 3D image format. The embedded physics named “emstandard” was used for the simulation of radiation transportation. The energy cut-off for radiation transport simulation was set to 0.1 keV for electrons and photons. To reduce the computation time, simulations were conducted only for 1% of the time-integrated activity, as in previous studies.<sup>10,27,28</sup> The statistical uncertainty of the dose estimation using 1% data was less than 3% at the voxel level. All simulations were performed with an in-house computing cluster with 60 CPU cores and 128 GB RAM.

## 2.3 | Multiple VSV approach

The detailed procedure for the multiple VSV approach was described in the previous work,<sup>10</sup> which is summarized in Figure 1. First, VSV kernels of <sup>177</sup>Lu in media with various densities were generated by GATE simulation. Each kernel had  $103 \times 103 \times 103$  dimensions with  $4.88 \times 4.88 \times 4.88 \text{ mm}^3$  voxel size. The dimension of the kernels was determined to sufficiently cover the dose range of <sup>177</sup>Lu. Each kernel was generated by performing GATE simulation with a <sup>177</sup>Lu point source distributed randomly in the single central voxel of media of different densities by defining the general point source (GPS). The activity of the single voxel source was  $10^8 \text{ Bq}$  the simulation time was 1 s. The generated kernels had units of  $\text{mGy}/(\text{MBq s})$ .

The second step involved the convolution of the time-integrated activity map with each kernel to produce medium-specific dose maps. The units of time-integrated activity maps and medium-specific doses were  $\text{MBq s}$  and Gy, respectively. Third, each medium-specific dose map was masked using binary medium masks, which were generated from CT-based density maps, as shown in Figure 1. Finally, all masked dose maps were summed to generate the final dose map. In the second step, kernel convolution was performed using a fast Fourier transform algorithm and a

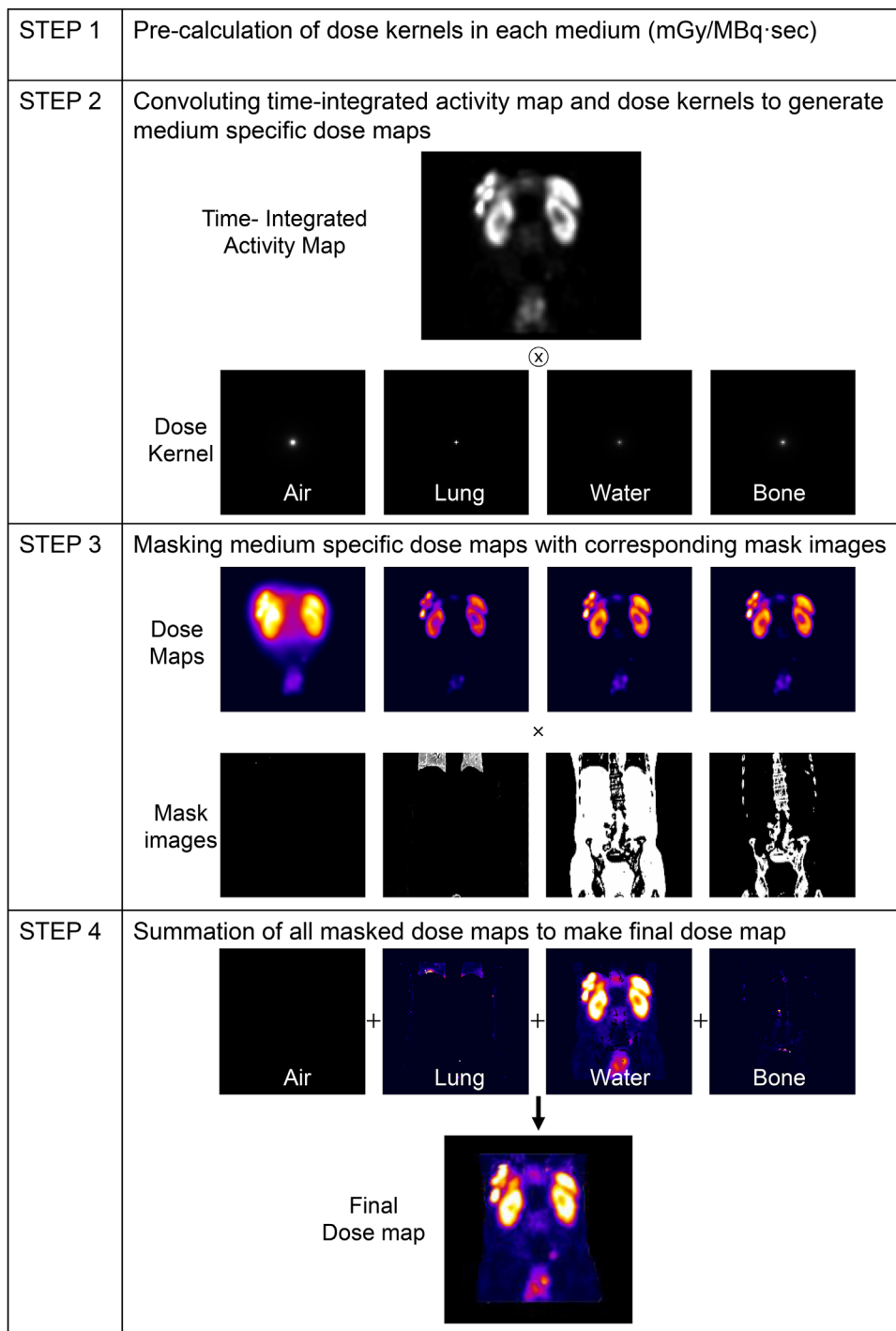


**FIGURE 1** Overview of the multiple voxel *S*-value (VSV) method

graphics processor unit (GPU, NVIDIA GeForce GTX 1080) in MATLAB 2021b.

In this study, the dose maps generated with four different VSV sets were compared with the reference method (dose map generated with Monte Carlo simulation). The media used for each VSV set are summarized in Tables S1 and S2. In brief, we included a conventional single VSV method ( $N = 1$ ) that considers the entire medium as water. For the  $N = 4$  case, we divided the medium into air,

lung, water, and bone. For the  $N = 10$  and 20 cases, more detailed soft tissue and bone densities were considered.

## 2.4 | Single VSV with density correction

The voxel-wise density correction for the single VSV method via a CT-based density map was performed as described previously.<sup>5,6</sup> Voxel-wise density maps were

generated from CT images by converting HU into density in  $\text{g}/\text{cm}^3$  with corresponding elemental compositions, as described earlier.<sup>26</sup> The ratio of water density ( $1 \text{ g}/\text{cm}^3$ ) to the actual density of each voxel was multiplied with the dose map estimated by applying a single VSV, as follows:

$$\text{Dose}_{\text{corr}}(x, y, z) (\text{Gy}) = \text{Dose}_{\text{VSV}}(x, y, z) \times \frac{\rho_{\text{water}}}{\rho_{\text{actual}}(x, y, z)} \quad (2)$$

## 2.5 | OLINDA/EXM

Organ-based dosimetry was performed using the OLINDA/EXM software.<sup>29</sup> For kidney and bone marrow dosimetry, the kidneys, bone marrow, liver, and spleen were considered the radioactive source organs. The time-integrated radioactivity in the remaining body was also calculated (i.e., total time-integrated activity minus the time-integrated activity of the source organs and metastatic tumors). The absorbed doses were corrected using the mass of each organ, as estimated by CT images. The total absorbed dose to red marrow ( $\text{Dose}_{\text{RM}}$ ) can be calculated as follows:

$$\text{Dose}_{\text{RM}} = \tilde{A}_{\text{RM}} \cdot S_{\text{RM} \leftarrow \text{RM}} + \tilde{A}_{\text{ROB}} \cdot S_{\text{RM} \leftarrow \text{ROB}} + \sum_h \tilde{A}_h \cdot S_{\text{RM} \leftarrow h} \quad (3)$$

where  $\tilde{A}_{\text{RM}}$ ,  $\tilde{A}_{\text{ROB}}$ , and  $\tilde{A}_h$  are the time-integrated radioactivity of red marrow, remainder of body (ROB), and other organs (kidneys, liver, and spleen) respectively. All organ-specific  $S$ -values provided in OLINDA/EXM were used.  $S_{\text{RM} \leftarrow \text{RM}}$ ,  $S_{\text{RM} \leftarrow \text{ROB}}$ , and  $S_{\text{RM} \leftarrow h}$  are the  $S$ -values for self-absorption of red marrow, cross-absorption from ROB, and other organs, respectively. The  $S$ -value of ROB was corrected for bone marrow dosimetry as performed in other work as follows<sup>17</sup>:

$$\begin{aligned} S_{\text{RM} \leftarrow \text{ROB}} = & S_{\text{RM} \leftarrow \text{TB,phantom}} \cdot \left( \frac{m_{\text{TB,phantom}}}{m_{\text{TB,patient}}} \right)^a \\ & \cdot \left( \frac{m_{\text{RM,phantom}}}{m_{\text{RM,patient}}} \right)^b - S_{\text{RM} \leftarrow \text{RM,phantom}} \\ & \cdot \left( \frac{m_{\text{RM,phantom}}}{m_{\text{ROB,patient}}} \right)^{0.992} - \sum_h S_{\text{RM} \leftarrow h, \text{phantom}} \\ & \cdot \left( \frac{m_{h,phantom}}{m_{\text{ROB,patient}}} \right) \cdot \left( \frac{m_{\text{RM,phantom}}}{m_{\text{RM,patient}}} \right) \quad (4) \end{aligned}$$

where  $S_{\text{RM} \leftarrow \text{RM,phantom}/\text{patient}}$ ,  $S_{\text{RM} \leftarrow \text{TB,phantom}/\text{patient}}$ , and  $S_{\text{RM} \leftarrow h, \text{phantom}/\text{patient}}$  are the  $S$ -values for self-absorption of red marrow, cross-absorption from total body, and other organs for the reference phan-

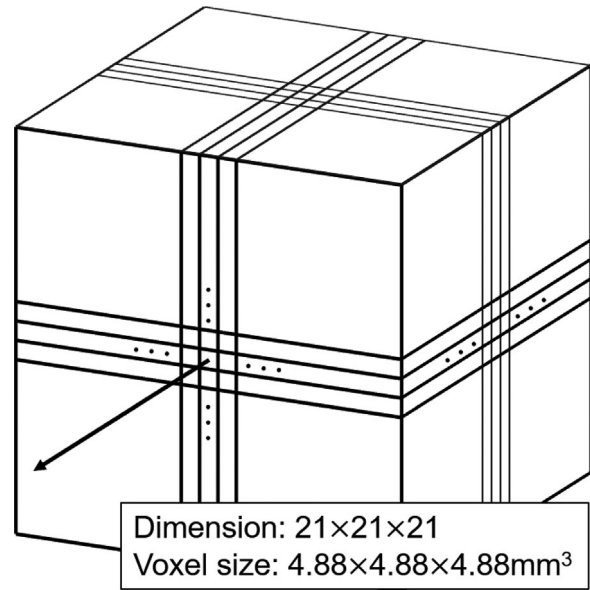


**FIGURE 2** The cubic phantom with  $21 \times 21 \times 21$  dimension and  $4.88 \times 4.88 \times 4.88 \text{ mm}^3$  voxel size used for phantom study

tom of OLINDA/EXM and real patients, respectively. And  $m_{\text{RM,phantom}/\text{patient}}$ ,  $m_{\text{TB,phantom}/\text{patient}}$ ,  $m_{\text{ROB,phantom}/\text{patient}}$ , and  $m_{h,phantom}/\text{patient}$  are the mass for red marrow, total body, ROB, and other organs for the reference phantom and real patients, respectively. The scaling factors  $a$  and  $b$  are different for male and female patients, where  $a = 0.896$  and  $b = 0.963$  for male and  $a = 0.894$  and  $b = 0.970$  for female patient.

In this study, the time-integrated activity and mass of VOIs of the lumbar spine without hard bone were used for  $\tilde{A}_{\text{RM}}$  and  $m_{\text{RM,phantom}}$ , respectively. The existence of trabecular bone and activity accumulation in cortical bone was not considered in this work.

For tumor dosimetry, the absorbed doses were calculated using a sphere model embedded in OLINDA/EXM. The comparison of emission spectrum of radiations from  $^{177}\text{Lu}$  used for GATE simulation and OLINDA/EXM is summarized in Table S3.<sup>30,31</sup>

## 2.6 | Additional Phantom study

The mathematical phantom study was conducted to investigate the difference between the multiple and the single VSV approaches with density correction. The  $21 \times 21 \times 21$  cubic phantom with  $4.88 \times 4.88 \times 4.88 \text{ mm}^3$  voxel size was used and each voxel was filled with  $10 \text{ kBq}$  of  $^{177}\text{Lu}$  as described in Figure 2. The dose rate profiles of center voxels were obtained using the Monte Carlo simulation, multiple VSV approach, and single VSV approach with density correction. The experiment was performed by changing the density of phantom (i.e., 1.2, 1.4, and  $1.6 \text{ g}/\text{cm}^3$ ).

## 2.7 | Estimation of absorbed dose

The absorbed dose in the kidney, bone marrow, and tumor regions was calculated as the mass-weighted averaged value within the VOIs. The total number of kidneys and bone marrow was 20 and 16, respectively. In addition, 133 tumor regions were included in the tumor dosimetry. Of these regions, 22 were bone-metastatic tumors. The mean absolute error (MAE) of each method ( $Dose_{est}$ ) and the reference method (Monte Carlo simulation) was calculated as follows:

$$MAE(\%) = \frac{1}{n} \sum_n \frac{|Dose_{est} - Dose_{MC}|}{Dose_{MC}} \times 100 \quad (5)$$

where  $n$  represents the number of data points. Furthermore, error maps in voxel level and dose volume histograms were generated to assess the differences in the voxel levels.

## 3 | RESULTS

### 3.1 | Monte Carlo simulation

The dosimetry measurements performed using each approach are summarized in Table 3. The time-integrated activity coefficients (i.e., the time-integrated activity divided by injection activity) were  $2.06 \pm 1.86$ ,  $0.13 \pm 0.36$ ,  $1.66 \pm 4.93$ , and  $0.14 \pm 0.10$  h for kidneys, bone marrow, tumor in soft tissue, and bone-metastatic tumor, respectively. The mean value of the kidney-absorbed doses (Gy) estimated using Monte Carlo simulation was  $9.07 \pm 2.83$ . The bone marrow dose was  $0.49 \pm 0.22$  when calculating the average dose after excluding four cases with bone metastasis in L-spine. The tumor dose was higher in the soft tissue than in the bone. Tumor doses in the soft tissue was  $31.22 \pm 28.85$  Gy and those in the bone was  $8.68 \pm 5.44$  Gy.

### 3.2 | Organ-based dosimetry

The error in estimating the absorbed dose using OLINDA/EXM compared to Monte Carlo simulation was high in bone marrow, as presented in the fifth columns of Table 3. The kidney dose error was approximately 5%, on average. However, the bone marrow error was 40.24%. The tumor dose, which was estimated using the sphere model that solely considered self-absorption, was significantly lower than the Monte Carlo estimate. The tumor dose estimation error was higher in the bone (6.04%) than in soft tissue (4.63%).

**TABLE 3** Absorbed dose (Gy) estimated using different dose estimation methods (mean ( $\pm$ standard deviation)) and mean absolute error (MAE, %) compared to Monte Carlo simulation for Sunway Medical Centre (SMC) data

Region	N	Dose (Gy)	MAE (%)	Monte Carlo	Organ S-value	Single VSV	4 VSVs	10 VSVs	20 VSVs	Single VSV <sub>corr</sub>
Kidney	20	Dose (Gy)		9.07 ( $\pm 2.83$ )	8.70 ( $\pm 2.80$ )	9.38 ( $\pm 2.92$ )	9.45 ( $\pm 2.87$ )	9.49 ( $\pm 2.88$ )	9.25 ( $\pm 2.87$ )	9.06 ( $\pm 2.83$ )
		MAE (%)		–	4.63	4.10	4.93	5.32	2.63	1.23
Bone marrow	16	Dose (Gy)		0.49 ( $\pm 0.22$ )	0.52 ( $\pm 0.49$ )	0.52 ( $\pm 0.24$ )	0.53 ( $\pm 0.24$ )	0.53 ( $\pm 0.24$ )	0.48 ( $\pm 0.22$ )	0.46 ( $\pm 0.21$ )
		MAE (%)		–	40.24	6.83	9.14	8.85	2.44	5.43
Tumor (soft tissue)	111	Dose (Gy)		31.22 ( $\pm 28.85$ )	30.09 ( $\pm 28.01$ )	33.25 ( $\pm 30.71$ )	33.38 ( $\pm 30.78$ )	33.42 ( $\pm 30.80$ )	30.84 ( $\pm 28.40$ )	31.51 ( $\pm 29.06$ )
		MAE (%)		–	4.63	6.06	6.70	6.92	2.71	0.98
Tumor (bone metastasis)	22	Dose (Gy)		8.68 ( $\pm 5.44$ )	8.28 ( $\pm 5.36$ )	9.88 ( $\pm 6.45$ )	9.89 ( $\pm 6.28$ )	10.00 ( $\pm 6.31$ )	9.08 ( $\pm 5.79$ )	8.83 ( $\pm 5.73$ )
		MAE (%)		–	6.04	12.90	11.19	12.74	4.08	1.52

Abbreviation: VSV, voxel S-value.

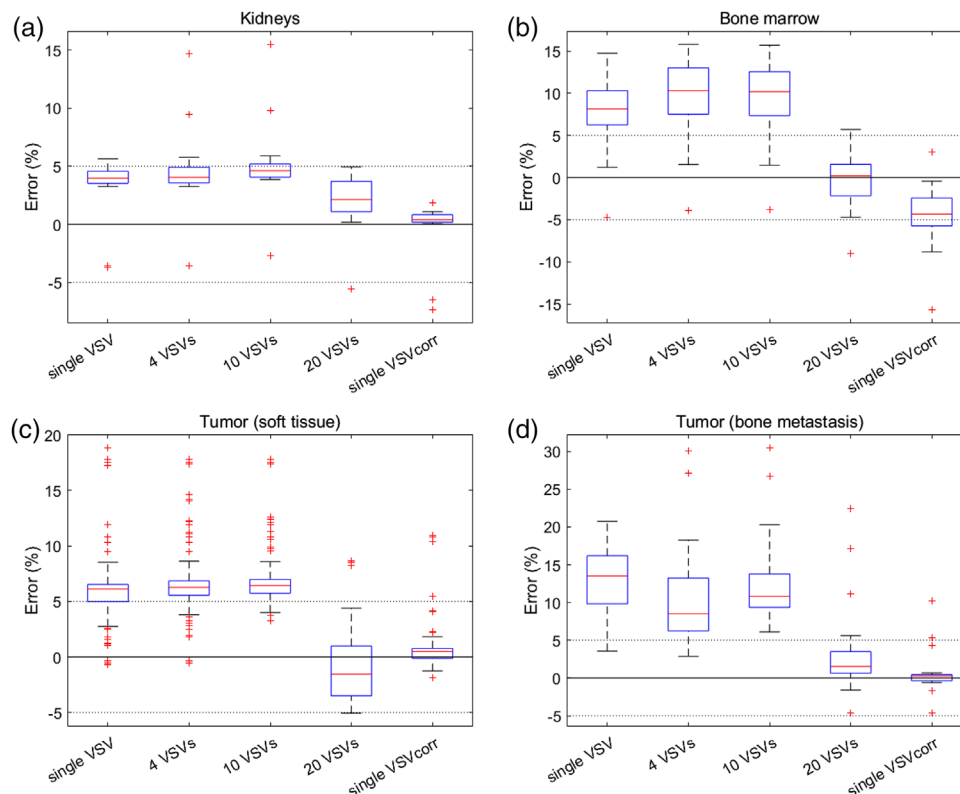


**FIGURE 3** Percentage error (box and whisker plots) of single and multiple voxel  $S$ -value (VSV) approaches with 20 VSV kernels compared to Monte Carlo simulation for the entire patient data. Error values outside the whiskers are indicated by (+)

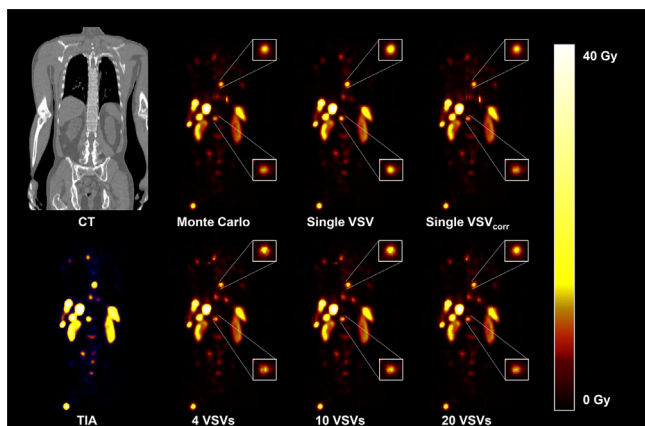


**FIGURE 4** Computed tomography (CT), time-integrated activity, and dose maps acquired using Monte Carlo simulation (the reference method) and voxel  $S$ -value (VSV) approaches

### 3.3 | VSV approaches

When a sufficient number of VSV kernels was adopted or density correction was applied to the single VSV approach, the dose estimates obtained via the VSV approaches were comparable to those obtained from the Monte Carlo simulation, as presented in Table 3, Figures 3–7, S3, and S4. Figure 3 shows the organ and tumor dose estimation errors for all patients, thus

indicating that the dose estimation error relative to the Monte Carlo simulation is minimal with a single VSV with density correction and 20 VSVs. VSVs fewer than 20 (1, 4, and 10 VSVs) yielded 4%–7% errors in kidney and soft tissue tumors predominated by water-equivalent tissue components (Figure 3a,c). However, as shown in Figure 3b,d, the error with VSVs less than 20 was remarkable in bone marrow and bone-metastatic tumors. The single VSV approach with density correction showed a smaller dose estimation error than the multiple VSV approach with 20 VSVs, except for the bone marrow (Table 3).

Figure 4 shows the dose maps generated using Monte Carlo simulation and VSV approaches from SPECT/CT images of a 52-year-old male patient diagnosed with rectal cancer who received 7.77 GBq  $^{177}\text{Lu}$ -DOTATATE at SMC. The enlarged regions indicate metastatic tumors in the thoracic spine and cervical spine. The tumor doses were overestimated with a single VSV without density correction; however, the overestimation was alleviated if more VSV kernels were employed or density correction was applied. In soft tissue organs (e.g., kidneys, spleen, and liver), the absorbed dose at the voxel level was similar regardless of the applied method. Figure 5 shows the relative and absolute dose error maps of a 49-year-old male patient diagnosed with pancreatic cancer who received 7.99 GBq  $^{177}\text{Lu}$ -DOTATATE. A metastatic tumor in the

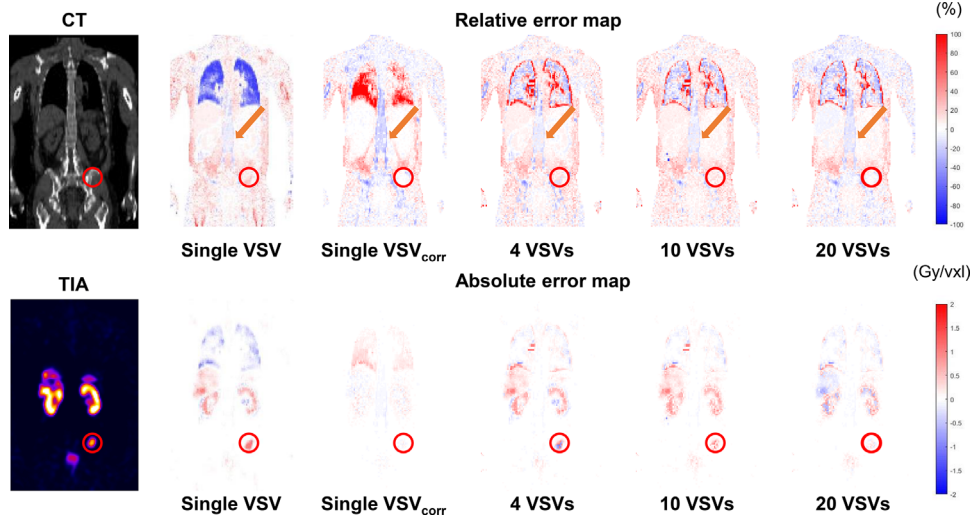


**FIGURE 5** Relative and absolute error maps of single voxel S-value (VSV) approach with density correction and multiple VSV approach compared to Monte Carlo simulation. Red circles indicate bone-metastatic tumors

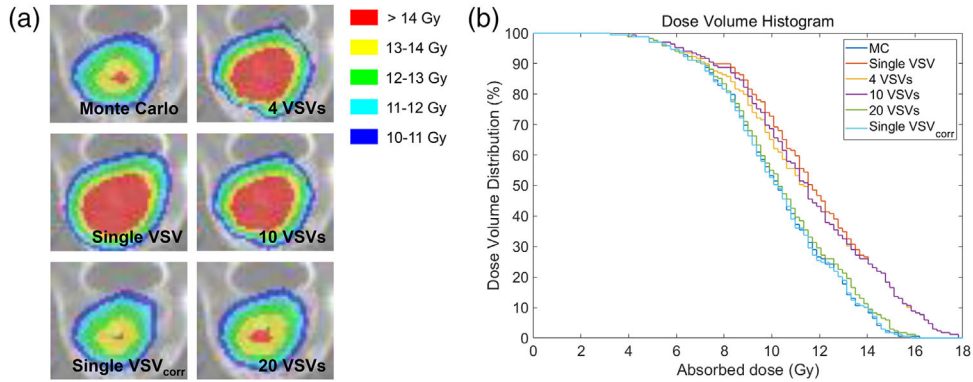


**FIGURE 6** Comparison of isodose maps and dose volume histograms on bone metastasis (thoracic spine) in a 54-year-old female patient diagnosed with rectal cancer and receiving 8.10 GBq <sup>177</sup>Lu-DOTATATE at Sunway Medical Centre (SMC). (a) Isodose maps acquired using Monte Carlo simulation (the reference method) and voxel S-value (VSV) approaches. (b) Dose volume histogram for the bone-metastatic tumor region shown in the isodose maps

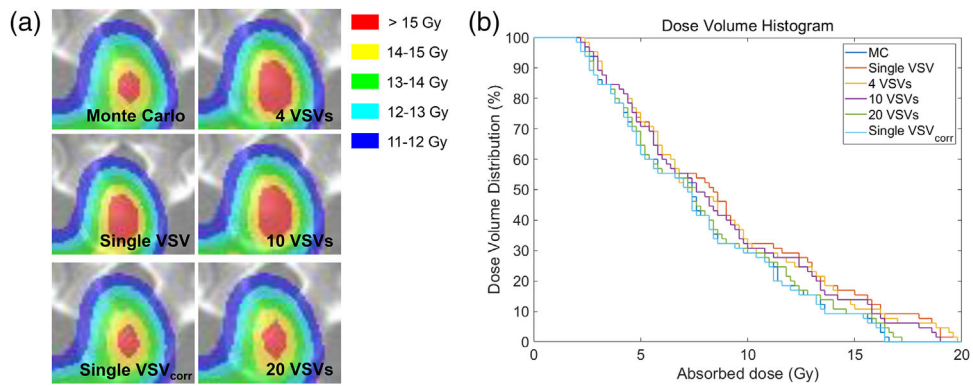


**FIGURE 7** Comparison of isodose maps and dose volume histograms on bone metastasis (pelvic bone) in an 84-year-old male patient diagnosed with lung cancer and receiving 8.07 GBq <sup>177</sup>Lu-DOTATATE at Sunway Medical Centre (SMC). (a) Isodose maps acquired using Monte Carlo simulation (the reference method) and voxel S-value (VSV) approaches. (b) Dose volume histogram for the bone-metastatic tumor region shown in the isodose maps

pelvic bone is indicated by red circles in each map. As more VSV kernels were used or density correction was applied, the dose error at the voxel level decreased. The error maps of various VSV approaches (single; 4, 10, and 20 VSVs; and single VSV with density correction) for other cases are also presented in Figures S3 and S4. A single VSV with density correction showed a larger error than 20 VSVs in the bone regions.

The accuracy of the VSV approaches is also demonstrated by isodose maps and dose volume histograms, as shown in Figures 6 and 7. The isodose map and dose volume histogram obtained using a single VSV with density correction and 20 VSVs were almost identical to those obtained with Monte Carlo simulation.

### 3.4 | Phantom study

The dose rate profiles at the center axial of the cubic phantom obtained using each method are shown in Figure 8. The dose underestimation by the single VSV approach with density correction was more significant as the density of the medium increased, whereas the multiple VSV provided similar results to the Monte Carlo simulation. The average differences of dose rate at center axial between the Monte Carlo simulation and the single VSV approach with density correction were -0.72%, -1.79%, and -2.36% in the 1.2, 1.4, and 1.6 g/cm<sup>3</sup> medium, respectively. In case of the multiple VSV approach, average differences were 0.54%, 0.49%, and 0.67% in the same order.

### 3.5 | Processing time for dosimetry

The image preprocessing including resampling and SPECT/CT co-registration took 10–20 min for each patient. The delineation of VOIs for each patient took about 15 min. The computation time required for the multiple VSV approach is much shorter than that required for Monte Carlo simulations. Although Monte Carlo simulations were performed for only 1% of the time-integrated activity, it took 70–80 h for each patient data using 60 CPU cores. However, 20 VSVs took only approximately 2 s with a six-core CPU, including image file I/O and dose map generation according to steps 2, 3, and 4, as summarized in Figure 1.

## 4 | DISCUSSION

In this first systemic report on voxel-based dose measurements for <sup>177</sup>Lu-DOTATATE, the accuracy of the different VSV approaches was evaluated in critical organs and primary and metastatic tumors. The 20 VSVs provided highly accurate results when compared to the Monte Carlo simulation, which is the reference method,

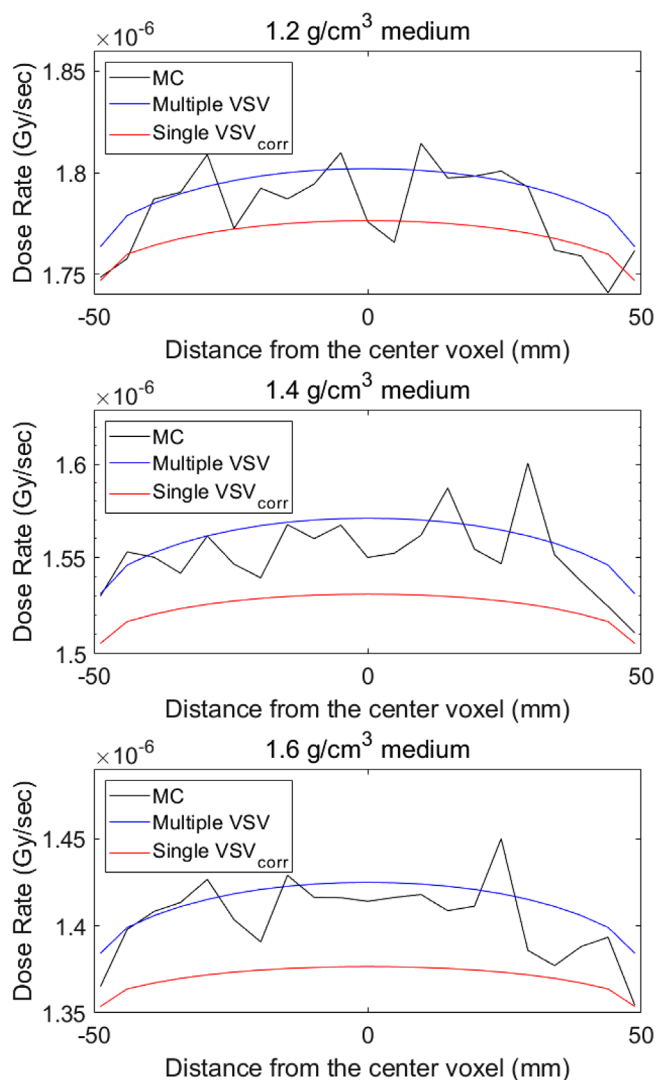


**FIGURE 8** The dose profiles obtained using the Monte Carlo simulation, multiple voxel S-value (VSV), and the single VSV approach with density correction at the center of the cubic phantom with various medium density

but required a long computation time. Kernel convolution was performed using a GPU-accelerated fast Fourier transform, which significantly reduced the computation time compared to the previous study.<sup>10</sup> Moreover, no remarkable artifacts were observed when applying 20 dose kernels. The average dose estimation error of the 20 VSVs for bone marrow was less than 6%, although the organ-based dosimetry using OLINDA/EXE yielded up to 123% error. The trend of increasing accuracy of the multiple VSV approach with a higher number of dose kernels was the same as that observed in our previous study conducted using <sup>68</sup>Ga-labeled RGD (Arg-Gly-Asp) agent based on 1,4,7-triazacyclononane-1,4,7-triacetic acid (<sup>68</sup>Ga-NOTA-RGD), which is a nontherapeutic radiopharmaceutical (Figure 3).<sup>10</sup> The advantages of the multiple VSV method over the organ-based dosimetry and the single VSV method were most

evident in bone marrow and bone-metastatic tumors (Table 3, Figures 5, S3, and S4), which are denser than water and composed of heterogeneous tissues.

As already suggested,<sup>5,6</sup> the accuracy of the single VSV method was significantly improved by applying density correction (Table 3, Figures 3, 5, S3, and S4). The organ dose errors were slightly smaller than those of the multiple VSV approach with 20 VSVs, except for the bone marrow. Figures 5, S3, and S4 demonstrate the reliability of the single VSV method with density correction. This simple correction may work because the range of beta particles emitted from <sup>177</sup>Lu is very short and self-absorption is dominant. However, the absorbed dose estimated using the single VSV approach with density correction was underestimated compared to the Monte Carlo simulation, as indicated by the orange arrows in Figures 5, S3, and S4. Dose underestimation was most significant in the spine from which we drew bone marrow VOIs, resulting in a larger error of bone marrow dose than that achieved using the multiple VSV approach. The dose underestimation was also observed in the phantom study as shown in Figure 8. This result explains the dose underestimation of the single VSV approach with density correction indicated by the orange arrow in Figures 5, S3, and S4. Although the density correction could not completely mitigate the error in estimating dose delivery to bone regions, it provided accurate dose estimates in most voxels.

The higher error of bone marrow dosimetry using the organ-based dosimetry with OLINDA/EXM compared to the voxel-based dosimetry resulted from two major reasons: (1) the microstructure of bone marrow considered in OLINDA/EXM and (2) inappropriate *S*-value of ROB used for the bone marrow dosimetry. First, the *S*-value of red marrow in OLINDA/EXM ( $S_{\text{RM} \leftarrow \text{RM, phantom}}$ ) was derived considering the microstructure of actual bone marrow (i.e., red marrow, yellow marrow, and trabecular bone region).<sup>29,32</sup> However, the microstructure of bone marrow was not considered when performing the voxel-based dosimetry even for Monte Carlo simulation. Second, although the correction for the *S*-value of ROB was performed, the overestimation was observed for some patients. The masses of red marrow of these patients ( $m_{\text{RM, patient}}$  in Equation (4)) were significantly smaller than the mass of phantom ( $m_{\text{RM, phantom}}$  in Equation (4)). As a result, the fraction term ( $m_{\text{RM, phantom}}/m_{\text{RM, patient}}$ ) in Equation (4) was large and therefore  $S_{\text{RM} \leftarrow \text{WB}}$ . The cross-absorption form ROB was more than 85% for these patients, which was probably overestimated.

In some patients with L-spine bone metastasis (four patients), the bone marrow dose estimated using voxel-based dosimetry was higher than 2 Gy limits due to a high uptake in bone marrow in the L-spine and cross-absorption from nearby high-uptake voxels. When we excluded the patients whose voxel-based dose measurements in the bone marrow were affected by the cross-absorption from L-spine bone metastasis, the

dose per administered activity in the bone marrow was 0.06 mGy/MBq with 20 VSVs, similar to other results reported based on organ-based dosimetry.<sup>12,13,16–20</sup>

Meanwhile, the tumor dose estimation performed using the sphere model in OLINDA/EXM was not as accurate as the VSV approaches with 20 VSVs or single VSV with density correction, even for soft tissue tumors, as shown in the fifth columns in Table 3. The different geometry of the tumor from the spherical shape, heterogeneous tissue composition, and influence of cross-absorption are possible causes of this error. In particular, the spherical model could not consider cross-absorption from voxels adjacent to the tumor VOI. Although individual tumor dosimetry for <sup>177</sup>Lu-DOTATATE therapy has been studied previously,<sup>14,16,18,33–36</sup> few previous studies have provided accurate tumor doses through voxel-based dosimetry. Garkavij et al.<sup>36</sup> performed voxel-based dosimetry for <sup>177</sup>Lu-DOTATATE using SPECT/CT images; however, only the energy deposition in each pixel has been considered and only two SPECT/CT scans have been used. The tumor doses for <sup>177</sup>Lu-DOTATATE measured in this study and other studies are summarized in Table S4. However, a direct comparison of these values is not meaningful because the characteristics of the patients enrolled in these studies and tumor locations were different.

One of the limitations of this study is that the partial volume effects were not corrected when estimating organ and tumor doses, which is the same in some of studies listed in Table S4. However, the partial volume effect does not depend on the dose estimation method; therefore, it does not affect the accuracy of each method. Another limitation is that physical decay factor of <sup>177</sup>Lu was used for estimation of voxel-wise time-integrated activity map. This approach does not consider the actual biological decay of the radionuclide; therefore, the time-integrated activity in some voxels would be overestimated. However, the voxel-wise exponential extrapolation was error-prone due to noise in SPECT images and intrinsic inaccuracy of co-registration of SPECT/CT images.<sup>37</sup>

There are some existing studies on the bone marrow dosimetry considering the microstructure of bone marrow.<sup>7,38,39</sup> But it was assumed that the VOIs of bone marrow consist of only the active marrow in this study because the spatial resolution of SPECT/CT is not sufficient for analyzing the effect of microstructure. Although the fraction of each microstructure component could be used for the calculation of mass and cumulative activity of each component as the previous work,<sup>7</sup> it was not applied to our methods because it probably introduces additional uncertainties.

The well-known hurdle of voxel-based dosimetry is that sequential SPECT/CT imaging is demanded to acquire time-integrated activity information. This procedure makes patients visit the hospital several times and takes additional costs. To reduce the efforts, the

simplified dosimetry using a single measurement approach was suggested.<sup>40</sup> The approximated time-integrated activity using a single SPECT/CT image after 4 days of <sup>177</sup>Lu-DOTATATE injection provided the most similar results compared to the true time-integrated activity according to the study. This approach would be extended to voxel-wise activity approximation. However, it is not considered in this study as the SPECT/CT imaging at 48 h after injection was the latest imaging and the approximation with this image would result in undesirable uncertainty.

In this study, large patient-to-patient variability in tumor uptake was observed; however, no attempt was made to quantify the relation between the tumor-absorbed dose and treatment response. Therefore, the dose–response relation in <sup>177</sup>Lu-DOTATATE therapy, which is based on the proposed method,<sup>12,13,15,19</sup> needs to be further studied, along with an appropriate study design in terms of patient selection and tumor response estimation. In the past few years, deep-learning-based medical image processing and analysis methods have rapidly evolved. Several groups, including ours, have proposed various deep-learning strategies for internal dosimetry.<sup>41–43</sup> In addition, a comparison of VSV methods with deep-learning-based approaches is required.

## 5 | CONCLUSIONS

The mean value of the absorbed doses estimated using Monte Carlo simulation were  $9.07 \pm 2.83$ ,  $0.49 \pm 0.22$ ,  $31.2 \pm 28.85$ , and  $8.68 \pm 5.44$  Gy for kidneys, bone marrow, tumor in soft tissue, and bone-metastatic tumor, respectively. The corresponding time-integrated activity coefficients were  $2.06 \pm 1.86$ ,  $0.13 \pm 0.36$ ,  $1.66 \pm 4.93$ , and  $0.14 \pm 0.10$  h in the same order. The application of the single VSV method with density correction and multiple VSV method with 20 dose kernels to a sequential <sup>177</sup>Lu-DOTATATE SPECT/CT dataset enabled fast and accurate radiation dose estimation, especially in bone marrow and bone-metastatic tumors with heterogeneous medium properties.

Although we neglected the existence of microstructure of bone marrow and considered the physical decay of <sup>177</sup>Lu only when obtaining a time-integrated activity map, it is believed that these assumptions do not hinder the intrinsic accuracy of the voxel-based dosimetry used in this study. Accordingly, the voxel-based dosimetry methods will be useful for managing administration activity to prevent the adverse effects of <sup>177</sup>Lu-DOTATATE therapy and for investigating tumor dose responses to further optimize the therapeutic efficacy of <sup>177</sup>Lu-DOTATATE.

## ACKNOWLEDGMENTS

This work was supported by grants from the National Research Foundation of Korea (NRF) funded by

the Korean Ministry of Science and ICT (Grant No. 2020M2D9A1093989) and Sunway Medical Centre. The funding source was not involved in the study design, collection, analysis, or interpretation. No other potential conflict of interest relevant to this article was reported.

## CONFLICT OF INTEREST

The authors have no conflicts to disclose.

## DATA AVAILABILITY STATEMENT

Data available on request due to privacy/ethical restrictions.

## REFERENCES

1. Kwekkeboom DJ, de Herder WW, Kam BL, et al. Treatment with the radiolabeled somatostatin analog [<sup>177</sup>Lu-DOTA<sup>0</sup>,Tyr<sup>3</sup>]octreotate: toxicity, efficacy, and survival. *J Clin Oncol*. 2008;26(13):2124-2130. <https://doi.org/10.1200/JCO.2007.15.2553>
2. Hosono M, Ikebuchi H, Nakamura Y, et al. Manual on the proper use of lutetium-177-labeled somatostatin analogue (Lu-177-DOTA-TATE) injectable in radionuclide therapy. *Ann Nucl Med*. 2018;32(3):217-235. <https://doi.org/10.1007/s12149-018-1230-7>
3. Graves SA, Flynn RT, Hyer DE. Dose point kernels for 2,174 radionuclides. *Med Phys*. 2019;46(11):5284-5293. <https://doi.org/10.1002/mp.13789>
4. Bolch WE, Bouchet LG, Robertson JS, et al. MIRD pamphlet No. 17: the dosimetry of nonuniform activity distributions - Radionuclide S values at the voxel level. *J Nucl Med*. 1999;40(1):11s-36s.
5. Dieudonné A, Hobbs RF, Lebtahi R, et al. Study of the impact of tissue density heterogeneities on 3-dimensional abdominal dosimetry: comparison between dose kernel convolution and direct Monte Carlo methods. *J Nucl Med*. 2013;54:236-243. <https://doi.org/10.2967/jnumed.112.105825>
6. Brosch-Lenz J, Uribe C, Gosewisch A, et al. Influence of dosimetry method on bone lesion absorbed dose estimates in PSMA therapy: application to mCRPC patients receiving Lu-177-PSMA-I&T. *EJNMMI Phys*. 2021;8(1):26. <https://doi.org/10.1186/s40658-021-00369-4>
7. Gosewisch A, Ilhan H, Tattenberg S, et al. 3D Monte Carlo bone marrow dosimetry for Lu-177-PSMA therapy with guidance of non-invasive 3D localization of active bone marrow via Tc-99m-anti-granulocyte antibody SPECT/CT. *EJNMMI Res*. 2019;9(1):76. <https://doi.org/10.1186/s13550-019-0548-z>
8. Goetz TI, Lang EW, Prante O, et al. Three-dimensional Monte Carlo-based voxel-wise tumor dosimetry in patients with neuroendocrine tumors who underwent <sup>177</sup>Lu-DOTATOC therapy. *Ann Nucl Med*. 2020;34(4):244-253. <https://doi.org/10.1007/s12149-020-01440-3>
9. Pacilio M, Lanconelli N, Lo M S, et al. Differences among Monte Carlo codes in the calculations of voxel S values for radionuclide targeted therapy and analysis of their impact on absorbed dose evaluations. *Med Phys*. 2009;36(5):1543-1552. <https://doi.org/10.1118/1.3103401>
10. Lee MS, Kim JH, Paeng JC, et al. Whole-body voxel-based personalized dosimetry: the multiple voxel S-value approach for heterogeneous media with nonuniform activity distributions. *J Nucl Med*. 2018;59(7):1133-1139. <https://doi.org/10.2967/jnumed.117.201095>
11. Ljungberg M, Celler A, Konijnenberg MW, et al. MIRD Pamphlet No. 26: joint EANM/MIRD guidelines for quantitative Lu-177 SPECT applied for dosimetry of radiopharmaceutical therapy. *J Nucl Med*. 2016;57(1):151-162. <https://doi.org/10.2967/jnumed.115.159012>

12. Forrer F, Krenning EP, Kooij PP, et al. Bone marrow dosimetry in peptide receptor radionuclide therapy with [<sup>177</sup>Lu-DOTA<sup>0</sup>,Tyr<sup>3</sup>]octreotate. *Eur J Nucl Med Mol Imaging*. 2009;36(7):1138-1146. <https://doi.org/10.1007/s00259-009-1072-6>
13. Hagmarker L, Svensson J, Ryden T, et al. Bone marrow absorbed doses and correlations with hematologic response during <sup>177</sup>Lu-DOTATATE treatments are influenced by image-based dosimetry method and presence of skeletal metastases. *J Nucl Med*. 2019;60(10):1406-1413. <https://doi.org/10.2967/jnumed.118.225235>
14. Gupta SK, Singla S, Thakral P, Bal CS. Dosimetric analyses of kidneys, liver, spleen, pituitary gland, and neuroendocrine tumors of patients treated with <sup>177</sup>Lu-DOTATATE. *Clin Nucl Med*. 2013;38(3):188-194. <https://doi.org/10.1097/RLU.0b013e3182814ac1>
15. Sundlov A, Sjogreen-Gleisner K, Svensson J, et al. Individualised Lu-177-DOTATATE treatment of neuroendocrine tumours based on kidney dosimetry. *Eur J Nucl Med Mol Imaging*. 2017;44(9):1480-1489. <https://doi.org/10.1007/s00259-017-3678-4>
16. Wehrmann C, Senfleben S, Zachert C, Muller D, Baum RP. Results of individual patient dosimetry in peptide receptor radionuclide therapy with <sup>177</sup>Lu DOTA-TATE and <sup>177</sup>Lu DOTA-NOC. *Cancer Biother Radiopharm*. 2007;22(3):406-416. <https://doi.org/10.1089/cbr.2006.325>
17. Gosewisch A, Delker A, Tattenberg S, et al. Patient-specific image-based bone marrow dosimetry in Lu-177-[DOTA<sup>0</sup>,Tyr<sup>3</sup>]Octreotate and Lu-177-DKFZ-PSMA-617 therapy: investigation of a new hybrid image approach. *EJNMMI Res*. 2018;8(1):76. <https://doi.org/10.1186/s13550-018-0427-z>
18. Thakral P, Sen I, Pant V, et al. Dosimetric analysis of patients with gastro entero pancreatic neuroendocrine tumors (NETs) treated with PRCRT (peptide receptor chemo radionuclide therapy) using Lu-177 DOTATATE and capecitabine/temozolomide (CAP/TEM). *Br J Radiol*. 2018;91(1091):20170172. <https://doi.org/10.1259/bjr.20170172>
19. Seregini E, Maccauro M, Coliva A, et al. Treatment with tandem [<sup>90</sup>Y]DOTA-TATE and [<sup>177</sup>Lu] DOTA-TATE of neuroendocrine tumors refractory to conventional therapy. *Eur J Nucl Med Mol Imaging*. 2014;41(2):223-230. <https://doi.org/10.1007/s00259-013-2578-5>
20. Sandstrom M, Garske-Roman U, Granberg D, et al. Individualized dosimetry of kidney and bone marrow in patients undergoing <sup>177</sup>Lu-DOTA-octreotate treatment. *J Nucl Med*. 2013;54(1):33-41. <https://doi.org/10.2967/jnumed.112.107524>
21. Hindorf C, Glatting G, Chiesa C, Linden O, Flux G, EANM Dosimetry Committee. EANM Dosimetry Committee guidelines for bone marrow and whole-body dosimetry. *Eur J Nucl Med Mol Imaging*. 2010;37(6):1238-1250. <https://doi.org/10.1007/s00259-010-1422-4>
22. Fedorov A, Beichel R, Kalpathy-Cramer J, et al. 3D slicer as an image computing platform for the quantitative imaging network. *Magn Reson Imaging*. 2012;30(9):1323-1341. <https://doi.org/10.1016/j.mri.2012.05.001>
23. Jan S, Santin G, Strul D, et al. GATE: a simulation toolkit for PET and SPECT. *Phys Med Biol*. 2004;49(19):4543-4561. <https://doi.org/10.1088/0031-9155/49/19/007>
24. Klein S, Staring M, Murphy K, Viergever MA, Pluim JPW. elastix: a toolbox for intensity-based medical image registration. *IEEE Trans Med Imaging*. 2010;29(1):196-205. <https://doi.org/10.1109/TMI.2009.2035616>
25. Guerriero F, Ferrari ME, Botta F, et al. Kidney dosimetry in <sup>177</sup>Lu and <sup>90</sup>Y peptide receptor radionuclide therapy: influence of image timing, time-activity integration method, and risk factors. *Biomed Res Int*. 2013;2013:935351. <https://doi.org/10.1155/2013/935351>
26. Schneider W, Bortfeld T, Schlegel W. Correlation between CT numbers and tissue parameters needed for Monte Carlo simulations of clinical dose distributions. *Phys Med Biol*. 2000;45(2):459-478. <https://doi.org/10.1088/0031-9155/45/2/314>
27. Gupta A, Lee MS, Kim JH, et al. Preclinical voxel-based dosimetry through GATE Monte Carlo simulation using PET/CT imaging of mice. *Phys Med Biol*. 2019;64(9):095007. <https://doi.org/10.1088/1361-6560/ab134b>
28. Gupta A, Shin JH, Lee MS, et al. Voxel-based dosimetry of iron oxide nanoparticle-conjugated Lu-177-labeled folic acid using SPECT/CT imaging of mice. *Mol Pharmaceut*. 2019;16(4):1498-1506. <https://doi.org/10.1021/acs.molpharmaceut.8b01125>
29. Stabin MG, Sparks RB, Crowe E. OLINDA/EXM: the second-generation personal computer software for internal dose assessment in nuclear medicine. *J Nucl Med*. 2005;46(6):1023-1027.
30. Kondev F. Nuclear data sheets for A = 177. *Nuclear Data Sheets*. 2019;159:1-412. <https://doi.org/10.1016/j.nds.2019.100514>
31. Stabin MG, da Luz LC. Decay data for internal and external dose assessment. *Health Phys*. 2002;83(4):471-475. <https://doi.org/10.1097/00004032-200210000-00004>
32. Stabin MG, Eckerman KF, Bolch WE, Bouchet LG, Patton PW. Evolution and status of bone and marrow dose models. *Cancer Biother Radiopharm*. 2002;17(4):427-433. <https://doi.org/10.1089/108497802760363213>
33. Ilan E, Sandström M, Wassberg C, et al. Dose response of pancreatic neuroendocrine tumors treated with peptide receptor radionuclide therapy using <sup>177</sup>Lu-DOTATATE. *J Nucl Med*. 2015;56(2):177-182. <https://doi.org/10.2967/jnumed.114.148437>
34. Jahn U, Ilan E, Sandström M, Garske-Román U, Lubberink M, Sundin A. <sup>177</sup>Lu-DOTATATE peptide receptor radionuclide therapy: dose response in small intestinal neuroendocrine tumors. *Neuroendocrinology*. 2020;110(7-8):662-670. <https://doi.org/10.1159/000504001>
35. Jahn U, Ilan E, Sandström M, Lubberink M, Garske-Román U, Sundin A. Peptide receptor radionuclide therapy (PRRT) with <sup>177</sup>Lu-DOTATATE; differences in tumor dosimetry, vascularity and lesion metrics in pancreatic and small intestinal neuroendocrine neoplasms. *Cancers*. 2021;13(5):962. <https://doi.org/10.3390/cancers13050962>
36. Garkavij M, Nickel M, Sjogreen-Gleisner K, et al. <sup>177</sup>Lu-[DOTA<sup>0</sup>,Tyr<sup>3</sup>] octreotate therapy in patients with disseminated neuroendocrine tumors: analysis of dosimetry with impact on future therapeutic strategy. *Cancers*. 2010;116(4 suppl):1084-1092. <https://doi.org/10.1002/cncr.24796>
37. Dewaraja YK, Frey EC, Sgouros G, et al. MIRD pamphlet No. 23: quantitative SPECT for patient-specific 3-dimensional dosimetry in internal radionuclide therapy. *J Nucl Med*. 2012;53(8):1310-1325. <https://doi.org/10.2967/jnumed.111.100123>
38. Sgouros G, Stabin M, Erdi Y, et al. Red marrow dosimetry for radiolabeled antibodies that bind to marrow, bone, or blood components. *Med Phys*. 2000;27(9):2150-2164. <https://doi.org/10.1118/1.1288393>
39. Geyer AM, Schwarz BC, Hobbs RF, Sgouros G, Bolch WE. Quantitative impact of changes in marrow cellularity, skeletal size, and bone mineral density on active marrow dosimetry based upon a reference model. *Med Phys*. 2017;44(1):272-283. <https://doi.org/10.1002/mp.12002>
40. Hänscheid H, Lapa C, Buck AK, Lassmann M, Werner RA. Dose mapping after endoradiotherapy with <sup>177</sup>Lu-DOTATATE/DOTATOC by a single measurement after 4 days. *J Nucl Med*. 2018;59(1):75-81. <https://doi.org/10.2967/jnumed.117.193706>
41. Lee MS, Hwang D, Kim JH, Lee JS. Deep-dose: a voxel dose estimation method using deep convolutional neural network for personalized internal dosimetry. *Sci Rep*. 2019;9:10308. <https://doi.org/10.1038/s41598-019-46620-y>
42. Gotz TI, Schmidkonz C, Chen S, Al-Baddai S, Kuwert T, Lang EW. A deep learning approach to radiation dose estimation. *Phys Med Biol*. 2020;65:036007. <https://doi.org/10.1088/1361-6560/ab65dc>

43. Akhavanallaf A, Shiri I, Arabi H, Zaidi H. Whole-body voxel-based internal dosimetry using deep learning. *Eur J Nucl Med Mol Imaging*. 2021;48:670-682. <https://doi.org/10.1007/s00259-020-05013-4>

### SUPPORTING INFORMATION

Additional supporting information may be found in the online version of the article at the publisher's website.

**How to cite this article:** Kim KM, Lee MS, Suh MS, et al. Comparison of voxel S-value methods for personalized voxel-based dosimetry of  $^{177}\text{Lu}$ -DOTATATE. *Med Phys*. 2022;49:1888–1901.  
<https://doi.org/10.1002/mp.15444>